OPEN

In-situ fabrication of macroporous films for dye-sensitised solar cells: formation of the scattering layer and the gelation of electrolytes

Su-Jin Ha & Jun Hyuk Moon

Department of Chemical and Biomolecular Engineering, Sogang University, Seoul 121-742, South Korea.

Dye-sensitised solar cells (DSCs) are a promising substitute for conventional silicon solar cells. A scattering layer of submicrometer pores or particles has been widely introduced to achieve a high light-harvesting efficiency. However, many such fabrication processes require high temperatures and multiple steps to prepare the scattering layer. Here, we have developed an in-situ fabrication process for a macroporous (MP) scattering film. The macropores were formed inside the assembled cell via the dissolution of polystyrene (PS) spheres from a PS/TiO$_2$ composite layer caused by exposure to an electrolyte solution. Specifically, the in-situ MP scattering layer decreased the transmittance of the electrode film from 58% to below 1%. The DSCs using these MP scattering layers exhibited an increase in the efficiency of 22%. Moreover, the dissolution of the PS improved the cell stability because of the gelation of the electrolyte solution; the efficiency of the DSCs was maintained at 80% of its initial value after ageing for 20 days, whereas the efficiency of the bare-electrode DSCs was found to have decreased by 50%. We believe that in-situ porous scattering layers show great promise for next-generation flexible DSCs. Moreover, this approach can be extended to various applications that utilize porous film/liquid systems.

Dye-sensitised solar cells (DSCs) are a promising substitute for conventional silicon solar cells because of their relatively high photon-to-electric efficiency and their low fabrication and materials costs[1,2]. A nanoparticlulate TiO$_2$ electrode film whose surface is functionalised by sensitising molecules (e.g., Ru-based dyes, organic dyes or recently perovskites) to permit the absorption of a wide range of sunlight wavelengths has been commonly used as a photon-absorbing electrode[1,3–8]. Upon exposure to light, the sensitisers absorb the light and release electrons into the TiO$_2$ electrode film[4]. Thus, a light-management strategy that maximises the optical density of the sensitized electrode is required to achieve high conversion efficiency. A simple approach is to utilise a thick electrode film; in this manner, the volumetric density of the sensitising dye molecules can be increased accordingly. However, this method is limited because the photogenerated electrons can only diffuse through a finite length due to the electron-hole (e.g., electrolyte ion) recombination[4]. The development of sensitising molecules that possess a large extinction coefficient and the capability of absorbing a wide range of wavelengths of light has been pursued as an alternative method. Recently, remarkable efficiency enhancement has been achieved using inorganic-organic hybrid perovskite structures that possess molar extinction coefficients that are approximately 10 times larger than those of the conventionally used Ru-based dye structures[6–8].

On the other hand, there is an indirect but facile and efficient approach to enhancing the efficiency by introducing optical scattering; the scattering enhances the optical density by elongating the optical path of the light inside the electrode film, thereby increasing the light absorption by the sensitised electrode film[9,10]. The size of the particles that comprise the conventional TiO$_2$ electrode film is approximately 20 nm; these particles induce only a weak Rayleigh scattering. Therefore, submicrometer particles or pores where the size is comparable to the wavelength of light are introduced to induce a strong Mie scattering[14,15]. It should be noted that most reported DSCs with an efficiency of greater than 10% have employed a submicrometer-sized particulate (PT) TiO$_2$ scattering layer on top of the electrode film[11–13]. Previously, the PT scattering layer have been formed by coating the TiO$_2$ particles either on top of the conventional electrode film or embedded in the electrode film[16–19]. The submicrometer pores have been produced via the selective removal of polymer spheres that had been incorporated into the electrode[20,21]. Many efforts have been made to optimise scatterer morphologies as well as the
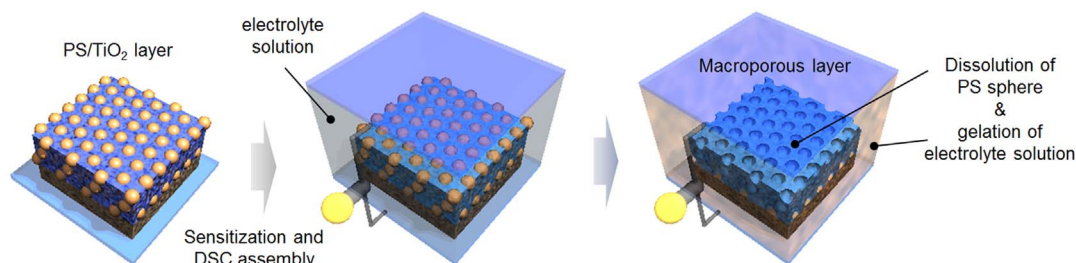
Figure 1 | In-situ fabrication of a macroporous scattering layer.

position of the scattering layer over the electrode film[10,16–22]. However, many of the fabrication processes for DSCs of this type require multiple steps to introduce the scattering layer, particularly, high temperature treatment.

In this paper, we demonstrate a novel approach to produce a submicrometer porous scattering layer for DSCs. This submicrometer layer was constructed using polymer sphere templates as similar to the previous approach[20,21], but the removal of polymer spheres was obtained inside the assembled DSCs. Thus, this approach allows low-temperature and in-situ fabrication of the porous scattering layer. Specifically, a mixed layer of submicrometer polystyrene spheres and TiO_2 nanoparticles was coated onto a conventional electrode film, and the in-situ dissolution of the polymer spheres caused by the introduction of an electrolyte solution inside the cell resulted in submicrometer cavities in the TiO_2 matrix. The macroporous scattering layer enhanced the photocurrent density by 19% and the efficiency by 22%, which was comparable to the performance of commercially available PT layer, although the fabrication was achieved at a low temperature and inside the cell. It should be also noted that this approach not only allows the in-situ fabrication of the porous layer but also promotes the enhancement of the cell stability through the formation of a physical gel electrolyte via the dissolution of the polymer spheres. The long-term stability of the DSCs was also enhanced by 60% in comparison with liquid-electrolyte DSCs through 20 days of ageing. This in-situ fabrication of a macroporous layer is facile and cost effective, and it is feasible for use in applications of next-generation DSCs, for example, flexible DSCs on plastic substrates. Moreover, this approach can be extended to various applications that utilize porous film/liquid systems, including photoelectrochemical devices, energy storage devices, microfluidics, and separation.

Results

In-situ formation of a macroporous scattering layer inside the assembled cell. Figure 1 shows the procedure for the in-situ formation of the macroporous (MP) scattering layer for DSCs. The polystyrene (PS)/TiO_2 nanoparticle composite layer was coated onto the top of the conventional nanoparticle (NP) TiO_2 electrode

film. Subsequently, these layers were sensitised with a conventional ruthenium-based dye (N719)[4]. The DSC was assembled by combining the dye-sensitised film with the counter electrode and subsequently injecting an electrolyte solution. At this time, the PS particles incorporated in the PS/TiO_2 layer were dissolved by the solvent of the electrolyte solution, which resulted in the creation of submicrometer macropores. Previously, the high-temperature process is required for the formation of a porous layer, whereby pores are produced by the removal of polymer particles that had been incorporated in the electrode layer. In contrast, our in-situ fabrication process, which self-produces the porous scattering layer inside the cell after cell assembly, allows low-temperature as well as one-step fabrication of the scattering layer.

Cross-sectional SEM images of the NP TiO_2 film (5 μm in thickness) and the PS/TiO_2 composite layer on the NP film are shown in Figure 2a and 2b, respectively. The PS/TiO_2 composite layer of 5 μm in thickness was formed by coating a colloidal mixture of TiO_2 particles and PS spheres (850 nm in diameter). Here, the TiO_2 colloids were prepared by mixing commercial anatase TiO_2 particles (P25, Degussa, average of 20 nm in diameter) and TiO_2 nanoparticles (average of 5 nm in diameter) that were synthesised through a sol-gel reaction (see Figure S1). The addition of TiO_2 nanoparticles was required to enhance the electron-transport properties of the TiO_2 scattering layer, which was prepared at low temperature[23]. Figure 2c shows a cross-sectional SEM image of the PS/TiO_2 composite film deposited on the NP TiO_2 film after the DSC assembly. Notably, the PS spheres were fully dissolved, which resulted in macropores with an approximate diameter of 800 nm in the TiO_2 film. Here, the real-time PS dissolution caused by the electrolyte solution was recorded by utilising PS spheres dyed with chlorophyll-a[24]. Figure 3 shows snapshot fluorescence images of the PS/TiO_2 composite layer after exposure to the electrolyte solvent, which was an acetonitrile/valeronitrile solution (85 : 15, v/v). The chlorophyll-a-dyed PS displayed a red colour upon UV excitation. Figure 3 reveals that after 60 s, the dissolution of PS spheres had begun, and it was completed at approximately 300 s. Here, the fraction of the PS mass to the solvent volume was estimated to be 8×10^{-3} mg/ml. We experimentally measured the solubility of the synthesised PS particles to be approxi-
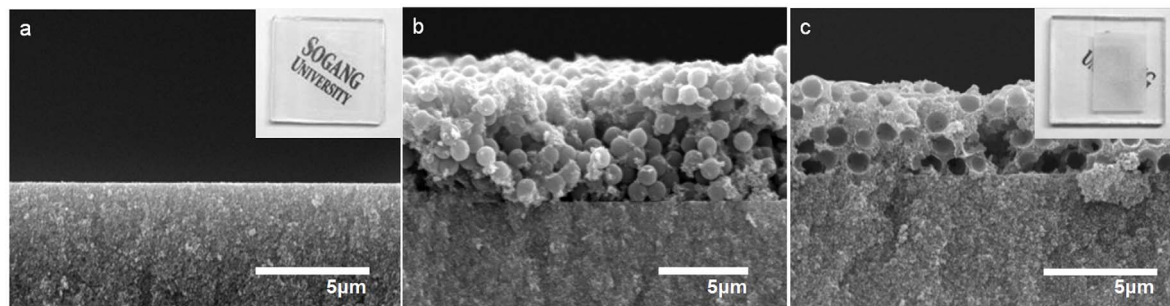
Figure 2 | Cross-sectional SEM images of (a) the conventional NP TiO_2 film, (b) the PS/TiO_2 composite layer on the NP film and (c) the MP TiO_2 film. The scale bars are 5 μm. The insets in figure a and figure c are photographs of each film on an FTO substrate (the area of the substrate is 2 cm*2 cm).

2
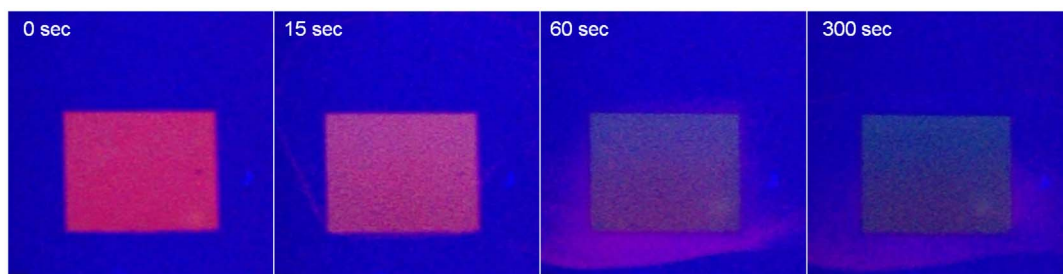
Figure 3 | Real-time fluorescence images of PS/TiO₂ composite layer after its exposure to the electrolyte solvent for the indicated duration.

mately 0.01 mg/ml in the acetonitrile/valeronitrile solution. Mean-while, the pore fraction could be directly controlled by the PS concentration in the PS/TiO₂ colloid mixture. Figure S2 shows surface SEM images of PS-dissolved TiO₂ films with different PS fractions. The areal fraction of the macropores on the surface was increased by increasing the PS content.

Optical properties of the macroporous scattering layer. In comparison with conventional TiO₂ electrode film (the inset image of Figure 2a), the addition of PS-dissolved TiO₂ makes the film more translucent because of the increased light scattering, as seen in the inset image of Figure 2c. A UV-Visible spectrometer was used to evaluate the light-scattering characteristics of the MP layer. First, we compared the transmittance and the diffuse reflectance spectra of the MP layers fabricated with low and high PS concentrations, as shown in Figure 4a and 4b, respectively. The diffuse reflectance and transmittance of the TiO₂ layer prepared without PS addition (i.e., non-porous) on the NP TiO₂ film were also measured for comparison. These layers were soaked with the acetonitrile/valeronitrile mixture to simulate the scattering behaviour inside the cell. While the non-porous/NP film exhibited a transmittance of 60% over the wavelength range of 400–700 nm, the low- and high-PS-dissolved MP films exhibited average transmittances of 1.5% and 0.5%, respectively. Accordingly, the diffuse reflectance of the PS-dissolved MP films increased with increasing macropore fraction. The low- and high-PS-dissolved MP films exhibited average diffuse reflectances of 25% and 30%, respectively, while the non-porous/ NP film displayed a reflectance of 10%. Thus, the low transmittance of these MP films is attributed to an increase in scattering. Meanwhile, considering the fact that the visible-light absorption by the TiO₂ film and the electrolyte solution was weak, the diffuse

reflectance of these films was relatively low, although little transmitted light was measured. Because the diffuse reflectance incorporates both the backward scattering by the film and the Fresnel reflection at the air/film interface, the difference between the diffuse reflectance and the normal transmittance yields the forward scattering. Thus, the relatively low reflectance is attributed to the forward scattering. The Mie scattering has a characteristic of strong forward scattering[14].

Secondly, the diffuse reflectance and transmittance of the PS-dissolved MP layers are also compared with those of a scattering layer prepared using commercially available particulates (PT scattering layer) in Figure 4a and 4b. The PT layer was composed of TiO₂ particles with an average diameter of 400 nm, and its thickness was controlled to be similar to that of the MP layer, as shown in Figure S3. In Figure 4a, the transmittance of the MP scattering layer averaged 0.5–1.5% over the measured wavelength range, and the PT scattering layer exhibited 0.3% transmittance. Figure 4b shows that the MP and the PT scattering layer averaged 30% and 35% reflectances over the measured wavelength range, respectively. These results may reveal that the MP layer possesses comparable scattering properties to the PT scattering layer. The low transmittance of these films in comparison with their reflectance was likewise attributed to forward scattering as mentioned above.

Scattering effect of the macroporous layer on the DSC efficiency. We characterised the effect of the MP scattering layer on the DSC efficiency and compared this effect to that of the PT scattering layer. First, the current-voltage (J-V) characteristics of the DSCs with or without the incorporation of the MP scattering layer on the conventional NP electrode are compared in Figure 5a. Table 1 lists the photovoltaic parameters of the short-circuit photocurrent
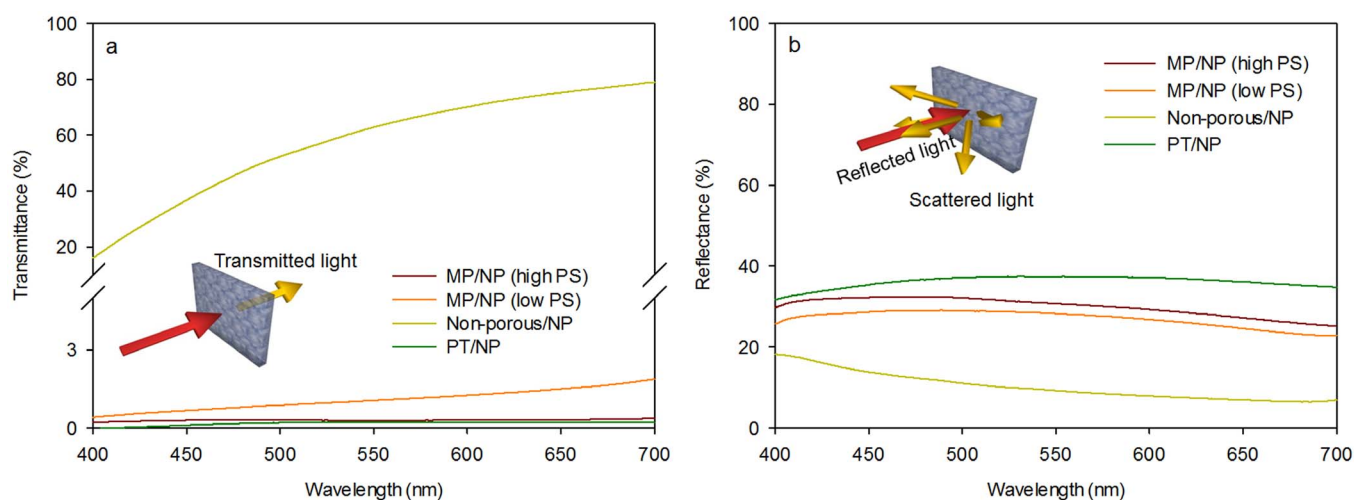
Figure 4 | (a), (b) Normal transmittance and diffuse reflectance of the non-porous/NP film, the MP layer with a low PS concentration and the macroporous layer with a high PS concentration. The normal transmittance and diffuse reflectance of the conventional particulate TiO₂ film is also shown.
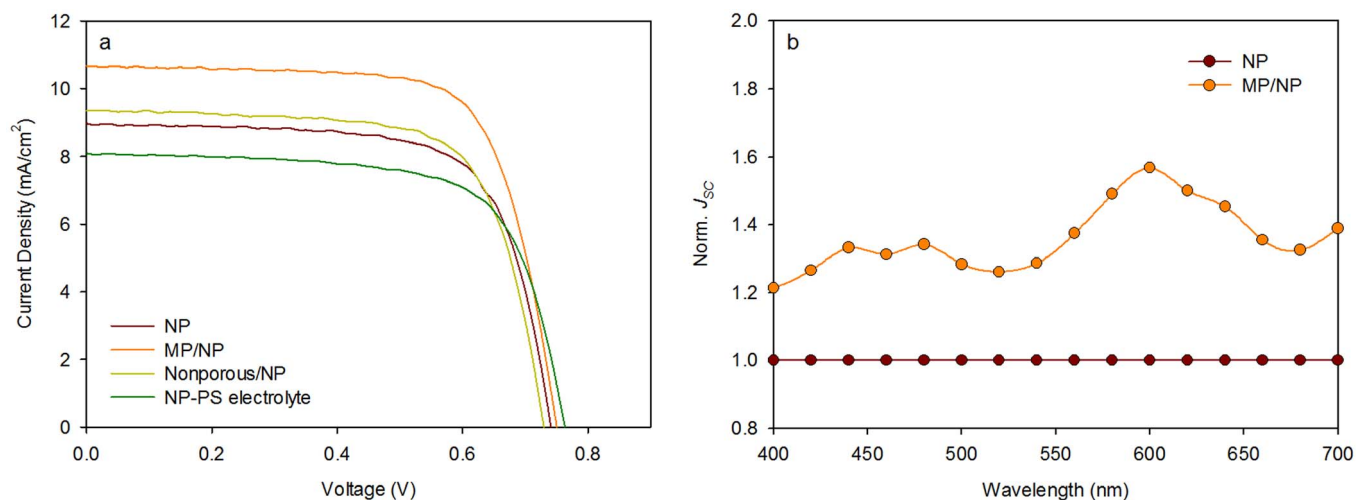
Figure 5 | (a) *J-V* characteristics of DSCs assembled using various electrode films. (b) The normalised J_{sc} measured at specific wavelengths for the MP/NP-electrode DSC. The normalisation was performed based upon the J_{sc} of the bare-NP-electrode DSC.

density (J_{sc}), the open-circuit voltage (V_{oc}), the fill factor (FF) from the *J-V* curve and the calculated photon-to-electric conversion efficiency. First of all, comparison of the *J-V* characteristics of the MP/NP electrode and the bare NP electrode demonstrates that the addition of the MP layer enhanced J_{sc} by 19%, from 8.97 mA/cm² to 10.67 mA/cm². This increase in J_{sc} can be attributed to the additional specific area and the scattering-enhanced light absorption contributed by the MP layer. Meanwhile, a nonporous layer prepared without PS incorporation was also prepared on an NP electrode, and their *J-V* characteristics are presented in Figure 5 and Table 1; the addition of this nonporous layer, which only increased the specific area of the electrode, increased J_{sc} by 4%. Thus, the additional 15% increase in J_{sc} observed for the MP layer can be attributed to the enhancement of the light absorption caused by the scattering of the MP layer. Figure 5b shows the J_{sc} values measured at specific wavelengths of light for the MP/NP-electrode DSCs normalised to the J_{sc} of the bare-NP-electrode DSC. In particular, a considerable enhancement was observed for the MP/NP-electrode cell in the wavelength range of 550–700 nm. This result confirms the J_{sc} enhancement attributable to both the light scattering of the MP layer and the increase in the specific area. Previously, scattering layers have effectively enhanced the light-harvesting efficiency for near-IR light wavelengths, where N719 molecules possess a low extinction coefficient[10,25].

Second, we evaluated the performance of the MP layer by comparing the characteristics of MP/NP-electrode and PT/NP-electrode DSCs. Because the scattering layer is a part of the electrode, the morphological characteristics (e.g., specific area) and the electron-transport properties should also be considered in addition to the scattering efficiency[10]. A large specific area is preferred for the attainment of higher sensitiser adsorptions. When the specific areas of the MP and PT TiO₂ films were compared by measuring the dye adsorption of these films, the MP layer was found to possess twice the dye-adsorption capability, or specific area (77 μmol/cm³), of the PT layer (40 μmol/cm³). The high specific area of the MP layer can be attributed to the fact that the macroporous matrix was composed of TiO₂ particle assemblies with mesopores around the particles, which is similar to the composition of the NP TiO₂ layer.

The photovoltaic performance of the MP/NP-electrode DSC is compared with the PT/NP-electrode DSC in Figure 5a and Table 1. In the case of the PT layer, J_{sc} was enhanced by 34%. This enhancement was approximately 15% greater than the J_{sc} enhancement caused by the MP scattering layer. Considering that the MP layer possessed twice specific area than the PT layer, this result was

unexpected. This may be attributed to the fact that the performance of the MP layer was obtained without the high-temperature treatment that was conducted to obtain the PT layer[26]. The heat treatment reduces defective sites of the TiO₂ particles as well as purifies the PT layer, which enhances the charge-transport properties and thereby improves the J_{sc}[27].

Meanwhile, the presence of PS in the electrolyte solution may have caused a loss of J_{sc} in the case of MP/NP-electrode DSC. Here, NP-electrode DSC was prepared with an electrolyte solution in which PS had been dissolved prior to its addition to the cell, and the performance of this cell was compared with that of the NP-electrode DSC without PS-dissolved electrolyte as also shown in Figure 5a and Table 1. It was observed that the J_{sc} value was decreased by 11% in the dissolved-PS-containing cell, which was attributed to the PS dissolution. Thus, it may be concluded that the MP layer, when considering the loss of J_{sc} by the dissolved PS, demonstrated a comparable J_{sc} enhancement to that of the conventional PT layer.

Effect of PS dissolution in the electrolyte solution on the photovoltaic parameters. The dissolution of PS in the electrolyte solution may result in the PS forming a physical gel with the solvent molecules[28,29]. A polymer-gelled electrolyte can be used to enhance the long-term stability of the DSCs[29–31]. In the case of liquid-electrolyte DSCs, the evaporation of the liquid solvent is difficult to prevent, and the loss of the solvent results in a loss of the photovoltaic parameters, increasing the operation time.

First, the effect of PS dissolution on the photovoltaic parameters was analysed via electrochemical impedance spectroscopy (EIS)[32,33]. We compared the EIS spectra of the NP-electrode DSCs with and without the MP layer, as shown in Figure 6. The DSC that contained the NP electrode with the PS-dissolved electrolyte was also investigated to confirm the effects of PS dissolution. The interfacial resistances were obtained by fitting the impedances using the equivalent

Table 1 | The photovoltaic parameters and calculated efficiencies of DSCs assembled using various electrode films

Sample	J_{sc} [mA/cm²]	V_{oc} [V]	FF	Eff. [%]
NP	8.97	0.75	0.70	4.71
MP/NP	10.67	0.75	0.72	5.76
Non-porous/NP	9.35	0.73	0.70	4.78
PT/NP	12.00	0.75	0.70	6.30
NP-PS electrolyte	8.10	0.76	0.69	4.25
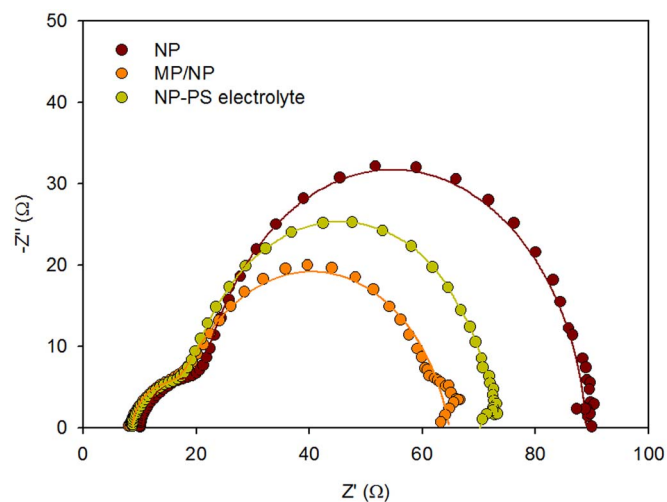
Figure 6 | Nyquist plot of the EIS measurements for DSCs assembled using various electrode films. The solid lines indicate the fitting results obtained for the equivalent circuit *R-R/CPE-R/CPE*.

Table 2 | The interfacial resistances of DSCs assembled using various electrode films

Sample	R_1	R_{ct}	R_2
NP	11.2	39.1	3.0
MP/NP	14.3	28.5	3.7
NP-PS electrolyte	14.2	35.2	3.9

circuit of R_1-R_{ct}/CPE-R_2/CPE; the resistances R_1, R_{ct} and R_2 are related to the electrochemical reactions at the Pt/electrolyte interfaces, the electrochemical reactions at the sensitised TiO$_2$/electrolyte interfaces and the diffusion of I$^-$ in the electrolytes, respectively, and they are listed in Table 2[32,33]. In comparison with the bare-NP-electrode DSC, the MP/NP-electrode DSC displayed an increase in R_2 and a decrease in R_{ct}. A similar change in these resistances was also observed in the NP-electrode cell with the PS-dissolved electrolyte. Thus, the dissolution of PS into the electrolyte solution decreases the diffusivity of electrolyte ion and increases the recombination reaction. It is reasonable to conclude that the gelation of the electrolyte by the PS increases the solution's viscosity and thereby decreases the ion diffusivity, and simultaneously, the slow diffusion of I$_3^-$ ions induces a higher rate of recombination reactions[29,34]. Meanwhile, the dissolution of PS in the electrolyte increased the value of R_1, and a similar increase was also observed in the NP electrode with the PS-dissolved electrolyte. The PS dissolution may have led to polymer adsorption on the counter electrode, which would increase the resistance.

Finally, the relative stability of the MP/NP-electrode DSC was evaluated; the photovoltaic parameters of the MP/NP- and bare-NP-electrode DSCs were recorded over time, as shown in Figure 7. It is notable that among the photovoltaic parameters, the J_{sc} of the liquid-electrolyte cell decreased considerably over time, whereas the NP/MP-electrode cell maintained its J_{sc}. The V_{oc} and FF values of both DSCs remained relatively stable. The J_{sc} of the NP-electrode cell with the PS-dissolved electrolyte was also maintained. These results support the hypothesis of the effective physical gelation of the dissolved PS and the liquid electrolyte as mentioned above. It should be noted that the NP/MP cell possessed superior stability in efficiency; after 20 days of ageing, 80% of the initial efficiency was maintained, whereas the liquid-electrolyte DSC maintained only 50% of its initial efficiency.

Discussion

We have developed an in-situ and low-temperature process for the dissolution of polystyrene (PS) spheres inside an assembled cell, which creates a porous scattering layer and simultaneously induces the gelation of the electrolyte solution, enhancing the light-harvesting efficiency and the stability of the DSC. We directly observed in-situ dissolution via florescence imaging. The transmittance and diffuse reflectance measurements indicated the occurrence of Mie scattering caused by the macroporous scattering layer; the macroporous TiO$_2$ scattering layer possessed comparable scattering efficiency to that of a conventional particulate scattering layer. Upon their application to DSCs, the macroporous scattering layers enhanced the photocurrent density of the DSCs by 19%, and the photon-to-electric conversion efficiency increased accordingly. It should be noted that this improvement was comparable to the improvement that has been reported in previous results, although our macroporous film was fabricated in-situ and using a low-temperature process. The dissolution of PS in the liquid electrolyte induced physical gelation, which enhanced the long-term stability of the DSCs. The long-term stability was enhanced by 60% with respect to liquid-electrolyte DSCs after duration of 20 days. Moreover, this in-site dissolution-induced gelation has the advantage of overcoming the difficulty of infiltrating the polymer gel electrolyte into the porous electrode. Further improvements in the macroporous morphologies, including the pore size and the pore density, as well as in the charge-transport properties of the TiO$_2$ matrix are expected to allow the development of a highly efficient low-temperature scattering layer. We believe this in-situ fabrication of a macroporous layer will prove advantageous for application to flexible-substrate DSCs, for which low-temperature processing is of critical importance. Moreover, this approach can be extended to various applications that utilize porous film/liquid systems, including photoelectrochemical devices (e.g. photocatalysts and water-splitting devices), various energy storage devices (e.g. supercapacitors), microfluidics, and separation.

Methods

Preparation of PS-dispersed TiO$_2$ colloid mixture and formation of PS/TiO$_2$ layer. A PS/TiO$_2$ colloid mixture was prepared by mixing polystyrene spheres, commercially available TiO$_2$ particles (P25, average diameter = 25 nm, Degussa) and synthesised TiO$_2$ nanoparticles with a volume ratio of 1 : 1 : 1–3 : 1 : 1. The monodispersed PS particles were synthesised via dispersion polymerisation using styrene (1 M in ethanol, Aldrich) as a monomer, 2,2′-azobis(2-methylbutyronitrile) as an initiator (1 wt% of monomer, Aldrich) and poly(N-vinylpyrrolidone) (10 g/L, Mw = 49,000, Junsei Chemicals Co.) as a stabiliser. The PS colloids were purified by washing with ethanol and were redispersed in ethanol at a concentration of 15 wt%. Meanwhile, TiO$_2$ nanoparticles were synthesised via a sol-gel reaction with a titanium (IV) isopropoxide precursor (TTIP, 97%, Aldrich). Briefly, 0.5 M TTIP was diluted in isopropanol (DAEJUNG) and added drop-wise into a 5%-acetic-acid/water solution for 12 hrs. Colloidal TiO$_2$ nanoparticles with an average diameter of 5 nm were obtained at a concentration of approximately 15 wt%. The commercial TiO$_2$ particles were dispersed in ethanol at a concentration of 15 wt%. The PS/TiO$_2$ colloid mixture was doctor-bladed onto the substrate and subsequently baked at 100°C for 1 hr.

Assembly of dye-sensitised solar cells. The TiO$_2$ film was cast onto the fluorine-doped SnO$_2$ (FTO) substrate and was sensitised by immersion in a dye solution, 0.5 mM N719 dye (Dyesol) in anhydrous ethyl alcohol (99.9%, Aldrich), for 40 hrs. The counter electrode was prepared by coating the FTO substrate with a 0.7 mM H$_2$PtCl$_6$ solution in anhydrous ethanol. The dye-sensitised TiO$_2$ electrode, with an active area of 13–15 mm^2, was assembled with the counter electrode, and the gap between the two electrodes was maintained using a 60-μm-thick polymer resin film (Surlyn, Dupont). Finally, the cell was filled with the redox electrolyte solution; the electrolyte solution was prepared by mixing 0.7 M 1-butyl-3-methylimidazolium iodide, 0.03 M iodine, 0.1 M guanidinium thiocyanate and 0.5 M tert-butylpyridine in a solution of acetonitrile and valeronitrile (85 : 15 v/v).

Characterisation. The surface/cross-section morphologies were measured via SEM (Hitachi). The fluorescence images were collected using a UV light source (365 nm, Vilber Lourmat) and a 500-nm long-pass filter (Thorlabs) with a digital camera. The transmission spectra were measured using a UV-Vis spectrometer (JASCO V550), and the diffuse reflectance was measured using the same spectrometer with an integrating sphere. The photocurrent and voltage of the DSCs were measured using a SourceMeter (Keithley Instruments) under simulated solar light that was produced by a 150 W Xe lamp (Oriel) and AM 1.5 G filters. The intensity of the lamp was adjusted
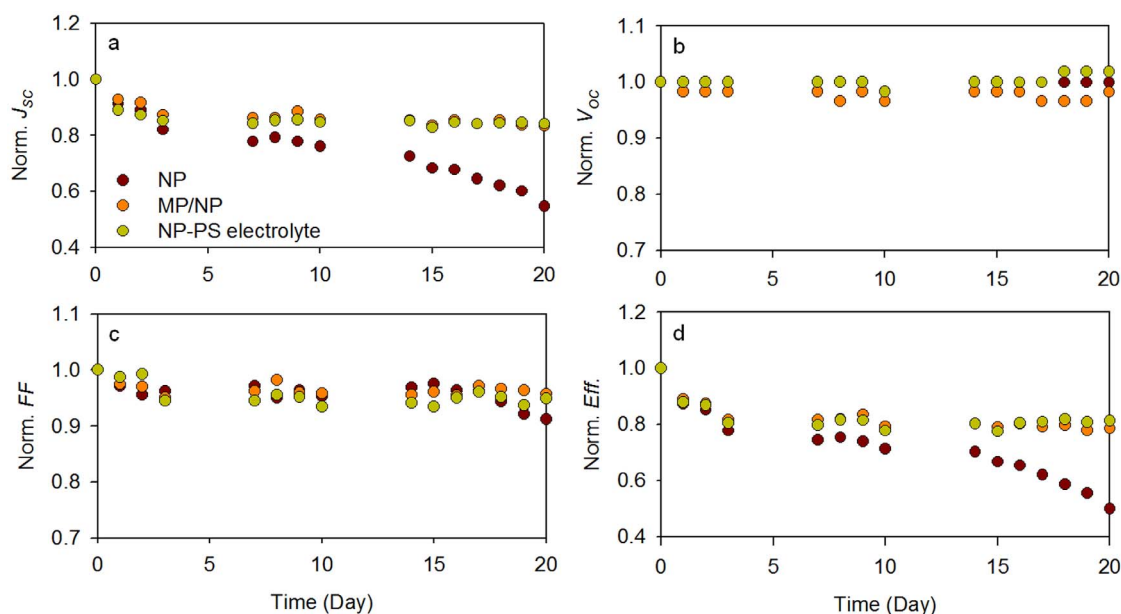
Figure 7 | Normalised photovoltaic parameters obtained during the long-term storage of DSCs assembled using various electrode films.

using a Si reference cell (BS-520, Bunko-Keiki) to a power density of 100 mW/cm². The impedance was measured using an impedance analyser (Versastat, AMETEK).

1. Oregan, B. & Gratzel, M. A low-cost, high-efficiency solar-cell based on dye-sensitized colloidal TiO₂ films. *Nature* **353**, 737–740, doi:10.1038/353737a0 (1991).

2. Hardin, B. E., Snaith, H. J. & McGehee, M. D. The renaissance of dye-sensitized solar cells. *Nat. Photon.* **6**, 162–169, doi:10.1038/nphoton.2012.22 (2012).

3. Grätzel, M. Recent Advances in Sensitized Mesoscopic Solar Cells. *Acc. Chem. Res.* **42**, 1788–1798, doi:10.1021/ar900141y (2009).

4. Hagfeldt, A., Boschloo, G., Sun, L. C., Kloo, L. & Pettersson, H. Dye-Sensitized Solar Cells. *Chem. Rev.* **110**, 6595–6663, doi:10.1021/cr900356p (2010).

5. Daeneke, T. *et al.* High-efficiency dye-sensitized solar cells with ferrocene-based electrolytes. *Nature Chem.* **3**, 211–215, doi:10.1038/nchem.966 (2011).

6. Burschka, J. *et al.* Sequential deposition as a route to high-performance perovskite-sensitized solar cells. *Nature* **499**, 316–319, doi:10.1038/nature12340 (2013).

7. Heo, J. H. *et al.* Efficient inorganic-organic hybrid heterojunction solar cells containing perovskite compound and polymeric hole conductors. *Nat. Photon.* **7**, 487–492, doi:10.1038/nphoton.2013.80 (2013).

8. Kim, H. S. *et al.* Mechanism of carrier accumulation in perovskite thin-absorber solar cells. *Nature Commun.* **4**, doi:10.1038/ncomms3242 (2013).

9. Ferber, J. & Luther, J. Computer simulations of light scattering and absorption in dye-sensitized solar cells. *Sol. Energ. Mater. Sol. Cell.* **54**, 265–275, doi:10.1016/s0927-0248(98)00078-6 (1998).

10. Enrique Galvez, F., Kemppainen, E., Miguez, H. & Halme, J. Effect of Diffuse Light Scattering Designs on the Efficiency of Dye Solar Cells: An Integral Optical and Electrical Description. *J. Phys. Chem. C* **116**, 11426–11433, doi:10.1021/jp2092708 (2012).

11. Gao, F. *et al.* Enhance the optical absorptivity of nanocrystalline TiO₂ film with high molar extinction coefficient ruthenium sensitizers for high performance dye-sensitized solar cells. *J. Am. Chem. Soc.* **130**, 10720–10728, doi:10.1021/ja801942j (2008).

12. Shi, D. *et al.* New Efficiency Records for Stable Dye-Sensitized Solar Cells with Low-Volatility and Ionic Liquid Electrolytes. *J. Phys. Chem. C* **112**, 17046–17050, doi:10.1021/jp808018h (2008).

13. Yella, A. *et al.* Porphyrin-Sensitized Solar Cells with Cobalt (II/III)-Based Redox Electrolyte Exceed 12 Percent Efficiency. *Science* **334**, 629–634, doi:10.1126/science.1209688 (2011).

14. Bohren, C. F. & Huffman, D. R. *Absorption and scattering of light by small particles.* (Wiley, New York, 1983).

15. Vargas, W. E. & Niklasson, G. A. Optical properties of nano-structured dye-sensitized solar cells. *Sol. Energ. Mater. Sol. Cell.* **69**, 147–163, doi:10.1016/s0927-0248(00)00388-3 (2001).

16. Wang, Z. S., Kawauchi, H., Kashima, T. & Arakawa, H. Significant influence of TiO₂ photoelectrode morphology on the energy conversion efficiency of N719 dye-sensitized solar cell. *Coord. Chem. Rev.* **248**, 1381–1389, doi:10.1016/j.ccr.2004.03.006 (2004).

17. Chen, D. *et al.* Synthesis of Monodisperse Mesoporous Titania Beads with Controllable Diameter, High Surface Areas, and Variable Pore Diameters (14–23 nm). *J. Am. Chem. Soc.* **132**, 4438–4444, doi:10.1021/ja100040p (2010).

18. Yu, I. G., Kim, Y. J., Kim, H. J., Lee, C. & Lee, W. I. Size-dependent light-scattering effects of nanoporous TiO₂ spheres in dye-sensitized solar cells. *J. Mater. Chem.* **21**, 532–538, doi:10.1039/c0jm02606a (2011).

19. Miao, X. H. *et al.* Controlled synthesis of mesoporous anatase TiO₂ microspheres as a scattering layer to enhance the photoelectrical conversion efficiency. *J. Mater. Chem. A* **1**, 9853–9861, doi:10.1039/c3ta11625e (2013).

20. Hore, S. *et al.* Scattering spherical voids in nanocrystalline TiO₂ - enhancement of efficiency in dye-sensitized solar cells. *Chem. Commun.* 2011–2013, doi:10.1039/b418658n (2005).

21. Thi, T. T. P. *et al.* Light scattering enhancement from sub-micrometer cavities in the photoanode for dye-sensitized solar cells. *J. Mater. Chem.* **22**, 16201–16204, doi:10.1039/c2jm32401f (2012).

22. Zhang, Q. F., Myers, D., Lan, J. L., Jenekhe, S. A. & Cao, G. Z. Applications of light scattering in dye-sensitized solar cells. *Phys. Chem. Chem. Phys.* **14**, 14982–14998, doi:10.1039/c2cp43089d (2012).

23. Li, Y. *et al.* Pure anatase TiO₂ "nanoglue": An inorganic binding agent to improve nanoparticle interconnections in the low-temperature sintering of dye-sensitized solar cells. *Appl. Phys. Lett.* **98**, doi:10330110.1063/1.3562030 (2011).

24. Lee, J. H., Gomez, I. J., Sitterle, V. B. & Meredith, J. C. Dye-labeled polystyrene latex microspheres prepared via a combined swelling-diffusion technique. *J. Coll. Interf. Sci.* **363**, 137–144, doi:10.1016/j.jcis.2011.07.047 (2011).

25. Hore, S., Vetter, C., Kern, R., Smit, H. & Hinsch, A. Influence of scattering layers on efficiency of dye-sensitized solar cells. *Sol. Energ. Mater. Sol. Cell.* **90**, 1176–1188, doi:10.1016/j.solmat.2005.07.002 (2006).

26. Wang, P. *et al.* Enhance the performance of dye-sensitized solar cells by Co-grafting amphiphilic sensitizer and hexadecylmalonic acid on TiO₂ nanocrystals. *J. Phys. Chem. B* **107**, 14336–14341, doi:10.1021/jp0365965 (2003).

27. Knorr, F. J., Zhang, D. & McHale, J. L. Influence of TiCl₄ treatment on surface defect photoluminescence in pure and mixed-phase nanocrystalline TiO₂. *Langmuir* **23**, 8686–8690, doi:10.1021/la700274k (2007).

28. Lee, K. S., Jun, Y. & Park, J. H. Controlled Dissolution of Polystyrene Nanobeads: Transition from Liquid Electrolyte to Gel Electrolyte. *Nano Lett.* **12**, 2233–2237, doi:10.1021/nl204287w (2012).

29. Nogueira, A. F., Durrant, J. R. & De Paoli, M. A. Dye-Sensitized Nanocrystalline Solar Cells Employing a Polymer Electrolyte. *Adv. Mater.* **13**, 826–830 (2001).

30. Hinsch, A. *et al.* Long-term stability of dye-sensitised solar cells. *Prog. Photovol.* **9**, 425–438, doi:10.1002/pip.397 (2001).

31. Kubo, W. *et al.* Quasi-solid-state dye-sensitized TiO₂ solar cells: Effective charge transport in mesoporous space filled with gel electrolytes containing iodide and iodine. *J. Phys. Chem. B* **105**, 12809–12815, doi:10.1021/jp012026y (2001).

32. van de Lagemaat, J., Park, N. G. & Frank, A. J. Influence of electrical potential distribution, charge transport, and recombination on the photopotential and photocurrent conversion efficiency of dye-sensitized nanocrystalline TiO₂ solar cells: A study by electrical impedance and optical modulation techniques. *J. Phys. Chem. B* **104**, 2044–2052, doi:10.1021/jp993172v (2000).

33. Fabregat-Santiago, F. *et al.* Correlation between Photovoltaic Performance and Impedance Spectroscopy of Dye-Sensitized Solar Cells Based on Ionic Liquids. *J. Phys. Chem. C* **111**, 6550–6560 (2007).

34. Asano, T., Kubo, T. & Nishikitani, Y. Electrochemical properties of dye-sensitized solar cells fabricated with PVDF-type polymeric solid electrolytes. *J. Photochem. Photobiol. a-Chem.* **164**, 111–115, doi:10.1016/j.jphotochem.2003.12.021 (2004).

Acknowledgments

Author contributions

S.H. designed and conducted the experiments. J.H.M. supervised the experiments. S.H. and J.H.M. contributed to the interpretation of the data and wrote the article.

Additional information